PHYSICAL REVIEW D **93,** 102002 (2016)

Study of statistical properties of hybrid statistic in coherent multidetector compact binary coalescences search

K. Haris[*] and Archana Pai[†]

Indian Institute of Science Education and Research Thiruvananthapuram, CET Campus, Trivandrum 695016, India

(Received 5 December 2015; published 9 May 2016)

In this article, we revisit the coherent gravitational wave search problem of compact binary coalescences with multidetector network consisting of advanced interferometers like LIGO-Virgo. Based on the loss of the optimal multidetector signal-to-noise ratio (SNR), we construct a hybrid statistic as a best of maximum-likelihood-ratio (MLR) statistic tuned for face-on and face-off binaries. The statistical properties of the hybrid statistic is studied. The performance of this hybrid statistic is compared with that of the coherent MLR statistic for generic inclination angles. Owing to the single synthetic data stream, the hybrid statistic gives few false alarms compared to the multidetector MLR statistic and small fractional loss in the optimum SNR for a large range of binary inclinations. We demonstrate that, for a LIGO-Virgo network and binary inclination $\epsilon < 70°$ and $\epsilon > 110°$, the hybrid statistic captures more than 98% of the network optimum matched filter SNR with a low false alarm rate. The Monte Carlo exercise with two distributions of incoming inclination angles—namely, $U[\cos\epsilon]$ and a more realistic distribution proposed by B. F. Schutz [Classical Quantum Gravity **28**, 125023 (2011)]—are performed with the hybrid statistic and give approximately 5% and 7% higher detection probabilities, respectively, compared to the two stream multidetector MLR statistic for a fixed false alarm probability of 10^{-5}.

DOI: 10.1103/PhysRevD.93.102002

I. INTRODUCTION

On September 14, 2015, the two Advanced LIGO detectors (LIGO-Livingston and LIGO-Hanford) [1,2] detected gravitational waves (GWs) for the first time from a binary black hole merger event [3]. The Advanced Virgo detector will be ready for observation of the cosmos very soon [4,5]. The Japanese cryogenic detector KAGRA is under construction [6,7], and a proposal for a detector in India—namely, LIGO-India—is in place [8]. Compact binary coalescences (CBCs) with neutron stars (NSs) and black holes (BHs) are one of the most promising GW sources for the Advanced LIGO–Virgo interferometric GW detectors. The Advanced LIGO detectors have a proposed distance reach of ∼445 Mpc for binary neutron star (BNS) events and are expected to detect a few BNS inspiral events per month [9]. Detection of CBCs would reveal information about the BHs as well as the NS equation of state. We expect many more surprises from nature in the form of GW detections, which would lead to a new, exciting field of GW astronomy in a few decades.

The detection of GWs in the interferometric data $\mathbf{x}$ is a statistical hypothesis testing problem, where the null hypothesis—$\mathbf{x}$ is purely the noise $\mathbf{n}$—is tested against an alternative hypothesis—$\mathbf{x}$ is the signal $\mathbf{s}$ plus the noise $\mathbf{n}$. The decision is based on construction of a *detection statistic*—a real valued function of $\mathbf{x}$—and is compared with a predefined threshold. When this test statistic crosses the threshold, the detection is declared. There are various strategies adopted for setting this threshold. The common strategy is to fix the *false alarm* rate (based on the available prior knowledge of the interferometer noise) and obtain the threshold value for the statistic.

The Neyman-Pearson lemma [10] says that the likelihood ratio (LR)—the probability ratio of the data following the alternative hypothesis and the null hypothesis—is the most powerful test statistic in cases of simple hypotheses (that is, the signal is known). However, for the GW detection problems, e.g., the CBC search or the continuous wave search (from a periodic source such as Pulsar), the signal model is known, but the parameters are unknown. Here, the alternative hypothesis is a composite hypothesis. There are two approaches to composite hypothesis testing. The first approach is the maximum-likelihood-ratio (MLR) approach, where the LR is maximized over the signal parameters. In the second approach—the Bayesian approach—which includes the astrophysical priors of the signal parameters, the LR is marginalized over the signal parameters with a prior distribution. For a high signal-to-noise ratio (SNR), the LR is expected to peak at the actual signal values in the multidimensional space of the signal parameters. Thus, most of the contribution to the marginalized LR is from the maximum. Therefore, the MLR statistic performs equally as well as the marginalized statistic in the high SNR regime.

The coherent multidetector search of GWs combines the incoming GW signal at different interferometers in a phase coherent way, where the information of the arrival time is

[*]haris@iisertvm.ac.in
[†]archana@iisertvm.ac.in

incorporated into the phase. The MLR based multidetector approach for the CBC signals is developed in the GW literature [11–13]. The nonspinning CBC signal is a function of nine parameters: namely, masses, source location, amplitude, binary inclination, polarization angle, phase at the time of arrival, and time of arrival at the reference detector. The MLR multidetector statistic obtained by maximizing the multidetector LR over a subset of four signal parameters (namely, amplitude, binary inclination, polarization angle, and initial phase) was shown to be the sum of a MLR statistic of two synthetic data streams which captures the two GW polarizations in Einsteinian general relativity. Henceforth, we will refer to this statistic as a generic MLR statistic. In [14], the authors investigate the performance of a multidetector MLR statistic devised for face-on/face-off binaries in the targeted follow-up of a short gamma ray burst (SGRB) in the GW window. In [15], the authors explore a Bayesian framework to address the multidetector CBC detection problem. The multidetector coherent approach for a continuous wave search is developed in [16] and [17], and the authors further compare the performance of the Bayesian vs MLR statistic in a specific set of amplitude coordinates given in [18].

In this paper, we revisit the MLR based multidetector CBC statistics. As mentioned above, the generic multidetector MLR statistic, $\mathcal{L}$, for the CBC signal is the sum of two single stream (synthetic data streams) MLR statistics [Eq. (2.38) of [12] and Eq. (44) of [13]] in the dominant polarization frame [19]. In this work, we carefully analyze the statistical properties of the multidetector MLR statistic for Gaussian noise. Furthermore, we obtain the MLR based statistics specially targeted for the face-on/face-off binaries which we denote as $\mathcal{L}^{0,\pi}$. This is a single data stream MLR statistic—as opposed to the two stream $\mathcal{L}$ statistic—and gives less false alarm rate as compared to that of $\mathcal{L}$. A careful study of SNRs of $\mathcal{L}^{0,\pi}$ indicates that either $\mathcal{L}^0$ or $\mathcal{L}^\pi$ captures most of the multidetector optimum SNR for a wide range of inclination angles, ϵ, and polarization angles, Ψ. We have demonstrated that, for $\epsilon < 70°$ and $\epsilon > 110°$, either $\mathcal{L}^0$ or $\mathcal{L}^\pi$ captures more than 98% of the network optimum matched filter SNR. This is one of the main results of the paper. We further constructed hybrid statistics, $\mathcal{L}^{mx} \equiv \max\{\mathcal{L}^0, \mathcal{L}^\pi\}$, and studied the statistical properties of the same for Gaussian noise. Pertaining to the single stream statistic capturing most of the optimum SNR, the hybrid statistic shows fewer false alarms than the two stream MLR statistic $\mathcal{L}$. We perform extensive numerical simulations to confirm the same. Furthermore, the *false alarm probability* (FAP) and the *detection probability* (DP) obtained from the simulations agree remarkably well with the proposed analytical expressions.

In [14], the authors examined the $\mathcal{L}^{0,\pi}$ statistic in the context of a targeted follow-up of SGRBs in GW windows. By comparing the inclination angle dependent polarization contributions to the SNR (i.e., $\cos\epsilon$ and $\frac{1+\cos^2\epsilon}{2}$), authors showed that face-on/face-off MLR statistics perform better (fewer false alarms) than the generic multidetector MLR statistic for the SGRB search. Since the focus was on the follow-up of SGRBs in the GW window, the observational constraints of the jet opening angle restricts the binary inclination angle within 30° from 0° or 180°. Thus, the study was restricted to the above mentioned range of binary inclinations. On the other hand, in this paper, we address generic inclination angles for the nonspinning CBC search.

The paper is organized as follows. In Sec. II, we review the nonspinning CBC signal, the multidetector MLR statistic $\mathcal{L}$, and the statistical properties of $\mathcal{L}$. In Sec. III, we construct the targeted face-on/face-off statistic $\mathcal{L}^{0,\pi}$ and study their statistical properties. We study the signal SNR in $\mathcal{L}^{0,\pi}$ for arbitrary inclination and polarization angles. In Sec. IV, we propose the hybrid statistic $\mathcal{L}^{mx}$ and study its statistical properties. In Sec. V, we summarize the numerical simulations and discuss the results.

II. REVIEW OF GW CBC COHERENT MULTIDETECTOR MLR STATISTIC

In this section, we summarize the earlier works [11–13] on the coherent multidetector MLR statistic for the detection of nonspinning CBC signals using advanced interferometers.

For a network of I interferometric detectors, the incoming GW signal from the nonspinning CBC source in the mth detector is denoted as $\mathbf{s}_m$. The signal is represented in the dominant polarization frame and in the frequency domain [13],

$$\tilde{s}_m(f) = \mathrm{A}\tilde{h}_0(f)e^{i\phi_a}\left[\left(\frac{1+\cos^2\epsilon}{2}\cos 2\chi + i\cos\epsilon\sin 2\chi\right)\mathrm{F}_{+m} + \left(\frac{1+\cos^2\epsilon}{2}\sin 2\chi - i\cos\epsilon\cos 2\chi\right)\mathrm{F}_{\times m}\right], \quad (1)$$

where the signal parameters are the overall amplitude A, initial phase ϕ_a (signal phase at the time of arrival in the fiducial reference detector typically coinciding with Earth's center), the binary inclination angle ϵ, and the polarization angle $\Psi = \chi - \delta/4$. The angle δ is a function of source direction and distribution of detectors on Earth, which uniquely defines the dominant polarization frame of the network for a given source direction. The $\mathrm{F}_m \equiv \mathrm{F}_{+m} + i\mathrm{F}_{\times m}$ is the complex antenna pattern function of the mth detector in the dominant polarization frame, which is a function of the source location and the multidetector configuration (the location of detectors on Earth's globe).[1] $\tilde{h}_0(f) \equiv f^{-\frac{7}{6}}e^{i\varphi(f)}$ defines the frequency evolution of the signal, with the restricted nonspinning 3.5 post-Newtonian phase $\varphi(f)$, which is a function of two component masses of the binary and the time of arrival of the signal in the

[1]Throughout the paper, we express the signal as well as the antenna pattern functions in the dominant polarization frame.

reference detector. Please note: here we assume that we know the source location (the targeted CBC search), and hence the signal $\mathbf{s}_m$ as defined in Eq. (1) is appropriately compensated for by the delays in the arrival time.

For spatially distributed detectors, the noise in an individual detector is independent. Thus, the network matched filter SNR square, $\boldsymbol{\rho}_s^2$, is the sum of the squares of SNRs in the individual detectors and is given by[2]

$$\boldsymbol{\rho}_s^2 = \sum_{m=1}^{I} \langle \mathbf{s}_m | \mathbf{s}_m \rangle. \tag{2}$$

A. Log-likelihood ratio

For interferometers with independent and additive Gaussian noise ($\mathbf{x} = \mathbf{s} + \mathbf{n}$), the network log-likelihood ratio (LLR), Λ, is the sum of the LLRs of the individual detectors [11,12],

$$2\Lambda = 2\sum_{m=1}^{I} \langle \mathbf{x}_m | \mathbf{s}_m \rangle - \langle \mathbf{s}_m | \mathbf{s}_m \rangle, \tag{3}$$

where $\mathbf{x}_m$ is the data stream from the mth detector. In [13], it is shown that Eq. (3) is the sum of the LLRs of two effective synthetic streams, $\mathbf{z}_L$ and $\mathbf{z}_R$, of the network:

$$2\Lambda = [2\boldsymbol{\rho}_L \langle \mathbf{z}_L | \mathbf{h}_0 e^{i\Phi_L} \rangle - \boldsymbol{\rho}_L^2] + [2\boldsymbol{\rho}_R \langle \mathbf{z}_R | \mathbf{h}_0 e^{i\Phi_R} \rangle - \boldsymbol{\rho}_R^2]. \tag{4}$$

For a given sky location, the overwhitened synthetic steams, $\tilde{\tilde{z}}_{L,R}(f)$, are obtained by projecting overwhitened network data on $+$ and $\times$ polarizations of the complex network antenna pattern vector in the dominant polarization frame as follows:

$$\tilde{\tilde{z}}_L(f) \equiv \sum_{m=1}^{I} \frac{\mathrm{F}_{+m}}{\|\mathbf{F}'_+\|} \tilde{\tilde{x}}_m(f), \qquad \tilde{\tilde{z}}_R(f) \equiv \sum_{m=1}^{I} \frac{\mathrm{F}_{\times m}}{\|\mathbf{F}'_\times\|} \tilde{\tilde{x}}_m(f). \tag{5}$$

The quantities $\|\mathbf{F}'_{+,\times}\|^2 = \sum_{m=1}^{I} g_m^2 \mathrm{F}_{+,\times m}^2$ incorporate the different noise PSDs in different detectors through $g_m^2 = \langle \mathbf{h}_0 | \mathbf{h}_0 \rangle$. g_m depicts the difference in individual SNRs of detectors caused by the difference in the noise PSD.

In this notation, the physical parameters $(\mathrm{A}, \phi_a, \epsilon, \Psi)$ are mapped to a new set of parameters $(\boldsymbol{\rho}_L, \boldsymbol{\rho}_R, \Phi_L, \Phi_R)$ as shown in Appendix A. Similar to the physical parameters, the new set of parameters appears to be carrying the extrinsic nature, as expected. From Eqs. (1), (2), and (A1), the multidetector matched filter SNR square is distributed in the individual synthetic stream SNRs, $\boldsymbol{\rho}_{Ls}$ and $\boldsymbol{\rho}_{Rs}$, as follows:

$$\boldsymbol{\rho}_s^2 = \boldsymbol{\rho}_{Ls}^2 + \boldsymbol{\rho}_{Rs}^2, \tag{6}$$

where the subscript s refers to the signal.

B. Maximization of LLR over extrinsic parameters

The multidetector MLR is obtained by maximizing LLR over the new parameters $(\boldsymbol{\rho}_L, \boldsymbol{\rho}_R, \Phi_L, \Phi_R)$ and is given in Eq. (44) of [13] as

$$\mathcal{L} \equiv 2\hat{\Lambda} = \underbrace{\langle \mathbf{z}_L | \mathbf{h}_0 \rangle^2 + \langle \mathbf{z}_L | \mathbf{h}_{\pi/2} \rangle^2}_{\hat{\boldsymbol{\rho}}_L^2} + \underbrace{\langle \mathbf{z}_R | \mathbf{h}_0 \rangle^2 + \langle \mathbf{z}_R | \mathbf{h}_{\pi/2} \rangle^2}_{\hat{\boldsymbol{\rho}}_R^2}. \tag{7}$$

$\mathcal{L}$ can be understood as the sum of power of the synthetic streams $\tilde{\mathbf{z}}_L$ and $\tilde{\mathbf{z}}_R$ in two quadratures, $\mathbf{h}_{0,\pi/2}$. In the absence of noise, $\mathcal{L}$ is equal to the multidetector matched filter SNR square [11–13] and, furthermore,

$$\hat{\boldsymbol{\rho}}_L|_{\mathbf{n}=0} = \boldsymbol{\rho}_{Ls} \qquad \hat{\boldsymbol{\rho}}_R|_{\mathbf{n}=0} = \boldsymbol{\rho}_{Rs}. \tag{8}$$

C. False alarm and detecton probabilities

In this section, we summarize the statistical properties of $\mathcal{L}$. Let $p_0(\mathcal{L})$ be the probability distribution of $\mathcal{L}$ in the absence of a signal and $p_1(\mathcal{L})$ be the distribution in the presence of a signal. For a given threshold £, the FAP, Q_0, and the DP, Q_d, are given by

$$Q_0(£) = \int_{£}^{\infty} p_0(\mathcal{L}) d\mathcal{L}, \quad Q_d(£) = \int_{£}^{\infty} p_1(\mathcal{L}) d\mathcal{L}. \tag{9}$$

In the absence of a signal and for uncorrelated Gaussian noise in the detectors, the four scalar products $\langle \mathbf{z}_{L,R} | \mathbf{h}_{0,\pi/2} \rangle$ in $\mathcal{L}$ are standard normal variates $\sim \mathcal{N}(0,1)$. Thus, with $\mathcal{L}$ being a sum square of four standard normal variates, it follows a χ^2 distribution with 4 degrees of freedom [11], i.e.,

$$p_0(\mathcal{L}) = \frac{\mathcal{L}}{4} \exp[-\mathcal{L}/2]. \tag{10}$$

The FAP becomes

$$Q_0(£) = \int_{£}^{\infty} p_0(\mathcal{L}) d\mathcal{L} = \left(1 + \frac{£}{2}\right) \exp[-£/2]. \tag{11}$$

[2]The scalar product of $\mathbf{a}$ and $\mathbf{b}$ is defined as

$$\langle \mathbf{a} | \mathbf{b} \rangle = 4\Re \int_0^{\infty} \tilde{\tilde{a}}(f) \tilde{b}^*(f) df,$$

where $\tilde{\tilde{a}}(f) = \tilde{a}(f)/S_n(f)$ is the double-whitened version of the frequency series $\tilde{a}(f)$. The $S_n(f)$ is the one sided noise power spectral density (PSD) of a detector.

In the presence of a signal, $\mathcal{L}$ is equal to the sum of the squares of four random variables following normal distribution with the unit variance and by individual means. Using Eq. (8), the sum of the squares of the means is equal to $\boldsymbol{\rho}_s^2$. Thus, the distribution of $\mathcal{L}$ follows [see Eq. (7.7) in [11]]:

$$p_1(\mathcal{L}) = \frac{1}{2}\frac{\mathcal{L}}{\boldsymbol{\rho}_s}\exp\left[-\frac{\mathcal{L}+\boldsymbol{\rho}_s^2}{2}\right] I_1(\boldsymbol{\rho}_s\sqrt{\mathcal{L}}), \tag{12}$$

where I_1 is the modified Bessel function of the first kind with the order 1. In an asymptotic limit $\boldsymbol{\rho}_s\sqrt{\mathcal{L}} \gg 1$, $p_1(\sqrt{\mathcal{L}})$ can be approximated by a Gaussian distribution [11],

$$p_1(\sqrt{\mathcal{L}}) = \frac{1}{2\pi}\exp\left[-\frac{(\sqrt{\mathcal{L}}-\boldsymbol{\rho}_s)^2}{2}\right]. \tag{13}$$

The DP can be approximated as

$$Q_d(\pounds) = \int_{\pounds}^{\infty} p_1(\mathcal{L})d\mathcal{L} \approx \frac{1}{2}\mathbf{erfc}\left(\frac{\sqrt{\pounds}-\boldsymbol{\rho}_s}{\sqrt{2}}\right), \tag{14}$$

where **erfc** is the complementary error function.

III. MAXIMUM-LIKELIHOOD ANALYSIS FOR FACE-ON/FACE-OFF SOURCES

In this section, we focus on the two special cases of the binaries—namely, face-on ($\epsilon = 0$) and face-off ($\epsilon = 180°$)—and obtain the MLR statistic.

From Eq. (1), the frequency domain signal for the face-on/face-off binary is given by

$$\tilde{s}_m^0(f) = \mathrm{A}\tilde{h}_0(f)\mathrm{F}_m^* e^{i(\phi_a+2\chi)}, \tag{15a}$$

$$\tilde{s}_m^\pi(f) = \mathrm{A}\tilde{h}_0(f)\mathrm{F}_m e^{i(\phi_a-2\chi)}. \tag{15b}$$

The superscript 0 and π correspond to the face-on and face-off cases, respectively. Please note that the polarization angle is absorbed in the initial phase. Hence, neither of the parameters can be estimated individually, which gives rise to a reduction in the parameter space by one. From Eq. (A1), the new parameters become

$$\boldsymbol{\rho}_L = \mathrm{A}\|\mathbf{F}'_+\|, \qquad \boldsymbol{\rho}_R = \frac{\|\mathbf{F}'_\times\|}{\|\mathbf{F}'_+\|}\boldsymbol{\rho}_L, \tag{16a}$$

$$\Phi_L = \chi + \phi_a, \qquad \Phi_R = \Phi_L \mp \frac{\pi}{2}. \tag{16b}$$

The only difference between the face-on and face-off cases appears in terms of a sign in Eq. (16b). In the expression of Φ_R, the negative sign is for the face-on case and positive for the face-off case, i.e., the Φ_R for the face-off gets shifted by 180° compared to the Φ_R in the face-off case. Please note that, in Eq. (16), $\boldsymbol{\rho}_R$ and Φ_R are expressed in terms of $\boldsymbol{\rho}_L$ and Φ_L. Thus, in the face-on/face-off case, LLR statistic is a function of two parameters instead of three. Physically, the face-on/face-off case amounts to the circular polarization, and hence different polarization angles carry no extra information and cannot be distinguished from the initial signal phase, ϕ_a.

If we substitute Eq. (16) into Eq. (4), the LLR reduces to

$$2\Lambda^{0,\pi} = 2\boldsymbol{\rho}\langle \mathbf{z}^{0,\pi}|\mathbf{h}_0 e^{i\Phi_L}\rangle - \boldsymbol{\rho}^2, \tag{17}$$

with the new parameter $\boldsymbol{\rho} \equiv \mathrm{A}\|\mathbf{F}'\|$ and

$$\tilde{z}^0(f) \equiv \sum_{m=1}^{I}\frac{\mathrm{F}_m}{\|\mathbf{F}'\|}\tilde{x}_m(f), \qquad \tilde{z}^\pi(f) \equiv \sum_{m=1}^{I}\frac{\mathrm{F}_m^*}{\|\mathbf{F}'\|}\tilde{x}_m(f). \tag{18}$$

Maximization of $\Lambda^{0,\pi}$ over $\boldsymbol{\rho}$ and Φ_L gives the MLR statistic $\hat{\Lambda}^{0,\pi}$ as

$$\mathcal{L}^{0,\pi} = \langle \mathbf{z}^{0,\pi}|\mathbf{h}_0\rangle^2 + \langle \mathbf{z}^{0,\pi}|\mathbf{h}_{\pi/2}\rangle^2. \tag{19}$$

The statistic is a single data stream statistic of $\mathbf{z}^{0,\pi}$, which is constructed in Eq. (18). $\mathcal{L}^{0,\pi}$ can be understood as the power of $\mathbf{z}^{0,\pi}$ in the two quadratures, $\mathbf{h}_{0,\pi/2}$. We expect the multidetector MLR statistic for the face-on/face-off case to evolve into such a single stream statistic since the signal is proportional to $\mathbf{F}^*$ or $\mathbf{F}$ [see Eq. (15)]. We note that Eq. (19) is the same as Eq. (22) of [14].

In the absence of noise, the statistics $\mathcal{L}^{0,\pi}$ becomes equal to the network matched filter SNR square, i.e.,

$$\mathcal{L}^{0,\pi}|_{\mathbf{n}=0} = \boldsymbol{\rho}_s^2. \tag{20}$$

A. False alarm and dismissal probabilities

In the absence of a signal, the scaler products $\langle \mathbf{z}^{0,\pi}|\mathbf{h}_0\rangle$ and $\langle \mathbf{z}^{0,\pi}|\mathbf{h}_{\pi/2}\rangle$ become standard normal variates. Thus, the probability distribution of $\mathcal{L}^0$ as well as $\mathcal{L}^\pi$ is χ^2, with 2 degrees of freedom, i.e.,

$$p_0(\mathcal{L}^{0,\pi}) = \frac{1}{2}\exp\left[-\mathcal{L}^{0,\pi}/2\right]. \tag{21}$$

The FAP with threshold $\pounds$ becomes

$$Q_0^{0,\pi}(\pounds) \equiv \int_{\pounds}^{\infty} p_0(\mathcal{L}^{0,\pi})d\mathcal{L}^{0,\pi} = \exp[-\pounds/2]. \tag{22}$$

In the presence of a signal, as in Sec. II C, $\mathcal{L}^{0,\pi}$ is equal to the sum of the squares of two Gaussian random variables with unit variance and distinct means, such that the sum of the squares is $\mathcal{L}^{0,\pi}|_{\mathbf{n}=0} = \boldsymbol{\rho}_s^2$. Then the distribution of $\mathcal{L}^{0,\pi}$ is given by Eq. (2.10) of [10] as

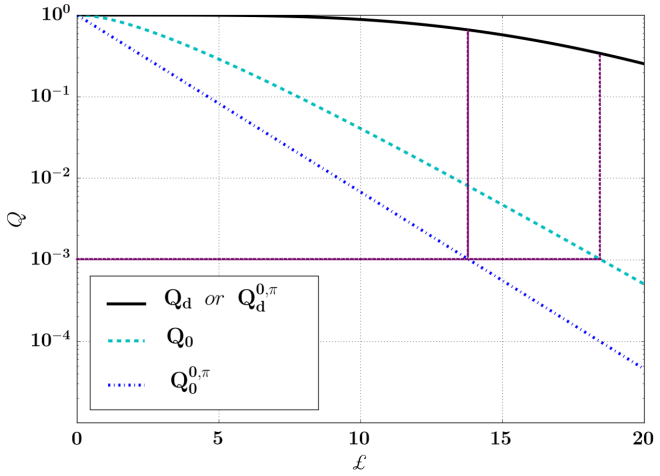

FIG. 1. Variation of the FAPs and the DPs of $\mathcal{L}$ and $\mathcal{L}^{0,\pi}$ with respect to the threshold £ for $\rho_s = 4$. For a fixed FAP of 10^{-3}, the DP of $\mathcal{L}^{0,\pi}$ is 0.67, while that of $\mathcal{L}$ is 0.35.

$$p_1(\mathcal{L}^{0,\pi}) = \frac{1}{2}\exp\left[-\frac{\mathcal{L}^{0,\pi}+\rho_s^2}{2}\right] I_0(\rho_s\sqrt{\mathcal{L}^{0,\pi}}), \qquad (23)$$

where I_0 is the modified Bessel function of the first kind with the order 0.

Similar to $\mathcal{L}$, in the asymptotic limit $\rho_s\sqrt{\mathcal{L}^{0,\pi}} \gg 1$, the distribution of $\sqrt{\mathcal{L}^{0,\pi}}$ can be approximated by a normal distribution with a mean equal to ρ_s and unit variance. Thus, the DP for the threshold £ can be approximated by the **erfc** function as

$$Q_d^{0,\pi}(£) \approx \frac{1}{2}\mathbf{erfc}\left(\frac{\sqrt{£}-\rho_s}{\sqrt{2}}\right). \qquad (24)$$

Here, we make an important observation that the DP of $\mathcal{L}^{0,\pi}$ in Eq. (24) is identical with the DP of $\mathcal{L}$ in Eq. (14) for a fixed multidetector optimum SNR ρ_s.

We remind the reader that now we have three distinct multidetector MLR statistics, namely, $\mathcal{L}$ for an unknown inclination angle and $\mathcal{L}^{0,\pi}$ targeting face-on/face-off sources. We note that the main difference between them is that $\mathcal{L}$ is a two data stream statistic, while $\mathcal{L}^{0,\pi}$ is a single stream statistic [see Eqs. (7) and (19)]. Thus, from the statistical properties [see Eqs. (11) and (22)], for a fixed threshold £ and a given signal SNR ρ_s, the false alarm rate of $\mathcal{L}$ would be higher than that of $\mathcal{L}^{0,\pi}$.

In other words, to achieve the fixed FAP, the threshold for $\mathcal{L}^{0,\pi}$ needs to be lower than that of $\mathcal{L}$. Therefore, more signal events will cross the threshold when the statistic $\mathcal{L}^{0,\pi}$ is used, as compared to $\mathcal{L}$. This makes $\mathcal{L}^{0,\pi}$ a better statistic compared to $\mathcal{L}$ in the face-on/face-off case. In Fig. 1, we have plotted the FAPs and DPs of $\mathcal{L}$ and $\mathcal{L}^{0,\pi}$ with respect to the threshold £ for $\rho_s = 4$. For example, when we draw a fixed FAP of the 10^{-3} line, the figure shows that the DP of $\mathcal{L}^{0,\pi}$ is 0.67, while that of $\mathcal{L}$ is 0.35, showing a clear improvement in the DP for $\mathcal{L}^{0,\pi}$.

B. Performance of $\mathcal{L}^{0,\pi}$ for an arbitrary inclination angle

In this section, we investigate the performance of $\mathcal{L}^{0,\pi}$ for an incoming signal from a binary with an arbitrary inclination. First, we study the fractional optimum SNRs captured by $\mathcal{L}^{0,\pi}$.

We note in the previous section that $\mathcal{L}^{0,\pi}|_{\mathbf{n}=0} = \rho_s^2$ for the face-on/face-off case. However, if we use the same statistic for an arbitrarily oriented binary, then the $\mathbf{z}^{0,\pi}$ would capture a fraction of the network matched filter SNR and it would drop with an increase in ϵ. We denote this fraction by $\omega^{0,\pi} \equiv \sqrt{\mathcal{L}^{0,\pi}}/\rho_s$.

In Appendix B, we derive the expression for $\omega^{0,\pi}$ and show that, for a wide range of ϵ's, either ω^0 or ω^π is close to one. Specifically, for $\epsilon \leq 70°$, $\omega^0 \approx 1$, and, for $110 \leq \epsilon \leq 180°$, $\omega^\pi \approx 1$. (Please see Appendix B for details.) This is elaborated in Fig. 2. It shows the behavior of ω^0 and ω^π with respect to ϵ for a network LHV, with Ligo-Livingston (L), Ligo-Hanford (H), and Virgo (V) as the constituent detectors. The signal is from a $(2-10M_\odot)$ NS-BH binary located at $(\theta = 140°, \phi = 100^0)$. We assume a fixed multidetector optimum SNR, $\rho_s = 6$. The plots are drawn for two different values of polarization angle, $\Psi = 0°$ and $\Psi = 45°$. We note that, for these values and for a fixed Ψ, the fraction $\omega^{0,\pi}$ captures most of the SNR for almost all values of ϵ, except for a window of 40° centered at $\epsilon = 90°$ (edge on case). Please note that the width of this window has a small variation with respect to Ψ, as shown in the figure.

In Fig. 3, we further elaborate the same by drawing the maps of ω^0 and ω^π in the $(\epsilon-\psi)$ plane [see Figs. 3(a) and 3(b)]. We draw contours of a constant $\omega^{0,\pi}$ at values $\omega^{0,\pi} = 0.98, 0.9, 0.8$. It is clear that $\forall\epsilon \leq 70°$ and, $\forall\Psi$,

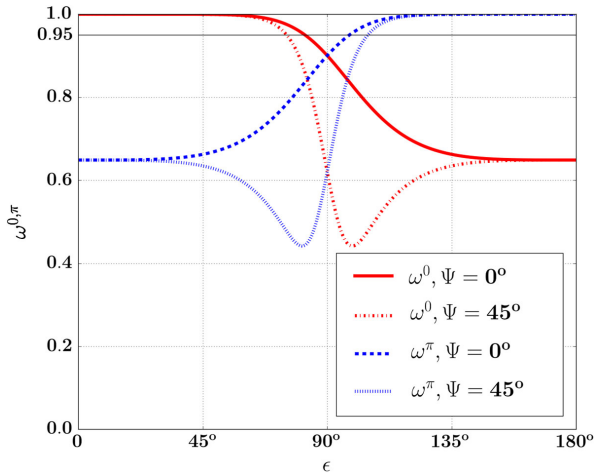

FIG. 2. Variation of ω^0 and ω^π with respect to the inclination angle ϵ for two different values of Ψ in the network LHV. The signal with the SNR $\rho_s = 6$ is from the $(2-10M_\odot)$ NS-BH system optimally located at $(\theta = 140°, \phi = 100°)$. We assume "zero-detuning, high power" Advanced LIGO PSDs for all detectors [20].

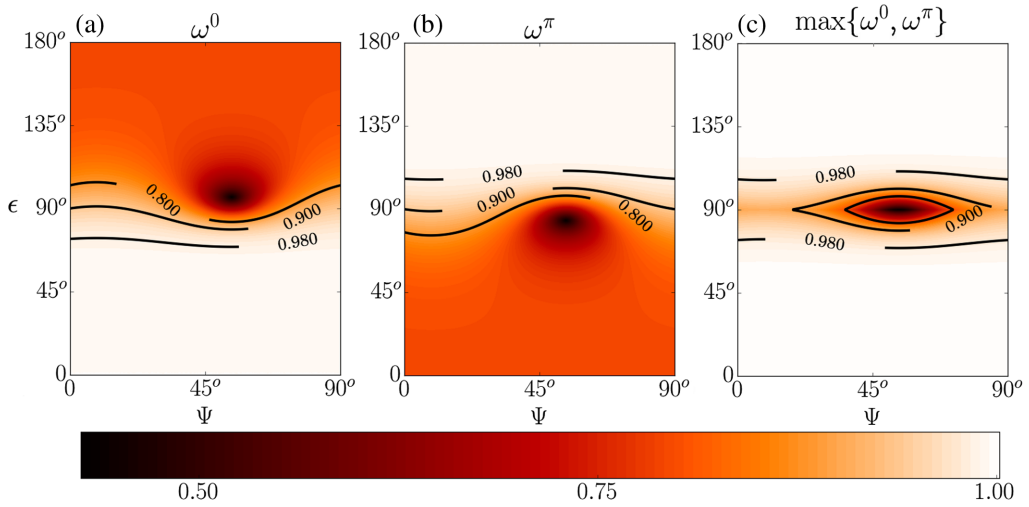

FIG. 3. (a) Map of ω^0 in the (ϵ, Ψ) plane for a network LHV. (b) Map of ω^π. (c) Map of $\max\{\omega^0, \omega^\pi\}$. The signal is from the $(2-10M_\odot)$ NS-BH system optimally located at $(\theta = 140°, \phi = 100°)$. The multidetector matched filter SNR, $\boldsymbol{\rho}_s = 6$. We assume zero-detuning, high power Advanced LIGO PSDs [20] for all detectors.

$\omega^0 \geq 0.98$. Similarly, for $110° \leq \epsilon \leq 180°$ and, $\forall\Psi$, $\omega^\pi \geq 0.98$. A small region of parameters with $70° < \epsilon < 110°$ shows a poor response to both $\mathbf{z}^0$ and $\mathbf{z}^\pi$. The ω^0 and ω^π are minimum at the point $(\epsilon = 90°, \chi = 45°)$. (Please note that $\chi = \Psi - \delta/4$, as defined in Sec. II.) We expect that the synthetic streams tuned for the face-on/face-off would give a poor response to the edge-on binary. Furthermore, we note that ω^0 and ω^π are complementary in nature about that $\epsilon = 90^0$. In Fig. 3(c), we draw the map of $\max\{\omega^0, \omega^\pi\}$. This shows that, barring a small region near the edge-on case, either $\mathbf{z}^0$ or $\mathbf{z}^\pi$ captures a large fraction of $\boldsymbol{\rho}_s$.

In the rest of the section, we comment on the statistical properties of $\mathcal{L}^{0,\pi}$ for an arbitrary inclination. The main difference for an arbitrarily oriented binary from the face-on/face-off case is that $\mathbf{z}^{0,\pi}$ captures a fraction of $\boldsymbol{\rho}_s$ instead of $\boldsymbol{\rho}_s$. Thus, in the presence of a signal, the distribution of $\mathcal{L}^{0,\pi}$ for an arbitrary ϵ is the same as Eq. (23), with $\boldsymbol{\rho}_s$ replaced by $\omega^{0,\pi}\boldsymbol{\rho}_s$:

$$p_1(\mathcal{L}^{0,\pi}) = \frac{1}{2}\exp\left[-\frac{\mathcal{L}^{0,\pi} + (\omega^{0,\pi}\boldsymbol{\rho}_s)^2}{2}\right] I_0\left(\omega^{0,\pi}\boldsymbol{\rho}_s\sqrt{\mathcal{L}^{0,\pi}}\right). \tag{25}$$

Furthermore, the DP remains the same as in Eq. (24), where $\boldsymbol{\rho}_s$ is replaced by $\omega^{0,\pi}\boldsymbol{\rho}_s$:

$$Q_d^{0,\pi}(\pounds) \approx \frac{1}{2}\,\mathbf{erfc}\left(\frac{\sqrt{\pounds} - \omega^{0,\pi}\boldsymbol{\rho}_s}{\sqrt{2}}\right). \tag{26}$$

Since FAP depends only on a noise model and the construction of a statistic, the FAP of $\mathcal{L}^{0,\pi}$ for an arbitrary inclination is the same as in Eq. (22).

As we discussed earlier, $\mathcal{L}^0$ captures more than 98% of $\boldsymbol{\rho}_s$ for $\epsilon \leq 70°$, while $\mathcal{L}^\pi$ captures more than 98% of $\boldsymbol{\rho}_s$ for $\epsilon \geq 110°$. Furthermore, Fig. 3 shows the complementary behavior of the two statistics $\mathcal{L}^0$ and $\mathcal{L}^\pi$. In addition, both $\mathcal{L}^0$ and $\mathcal{L}^\pi$ are constructed out of a single synthetic stream, as opposed to the $\mathcal{L}$ statistic (two streams). This motivates us to construct a hybrid statistic out of $\mathcal{L}^0$ and $\mathcal{L}^\pi$, which would capture most of the multidetector SNR for a large range of binary inclinations for the CBC search.

IV. PROPOSAL OF HYBRID STATISTIC $\mathcal{L}^{mx}$

In this section we propose a hybrid statistic as $\mathcal{L}^{mx} \equiv \max\{\mathcal{L}^0, \mathcal{L}^\pi\}$ and study its statistical properties.

In the absence of a signal, both $\mathcal{L}^0$ and $\mathcal{L}^\pi$ follow a χ^2 distribution with 2 degrees of freedom [see Eq. (21)]. Let $\mathbf{P}(\mathcal{L}^0, \mathcal{L}^\pi)$ be the joint probability distribution of $\mathcal{L}^0$ and $\mathcal{L}^\pi$. The probability distribution of $\mathcal{L}^{mx}$ can then be written

$$p_0(\mathcal{L}^{mx}) = 2\int_0^{\mathcal{L}^{mx}} \mathbf{P}(\mathcal{L}^0 = \mathcal{L}^{mx}, \mathcal{L}^\pi)d\mathcal{L}^\pi. \tag{27}$$

Please note that here $\mathcal{L}^0$ and $\mathcal{L}^\pi$ have nonzero covariance, i.e., they are not independent of each other.

In Eq. (B2), $\mathcal{L}^{0,\pi}$ is expressed in terms of $\mathbf{z}_{L,R}$ as

$$\mathcal{L}^{0,\pi} = \left(\frac{\|\mathbf{F}'_+\|}{\|\mathbf{F}'\|}\langle \mathbf{z}_L|\mathbf{h}_0\rangle \pm \frac{\|\mathbf{F}'_\times\|}{\|\mathbf{F}'\|}\langle \mathbf{z}_R|\mathbf{h}_\pi/2\rangle\right)^2 + \left(\frac{\|\mathbf{F}'_+\|}{\|\mathbf{F}'\|}\langle \mathbf{z}_L|\mathbf{h}_\pi/2\rangle \mp \frac{\|\mathbf{F}'_\times\|}{\|\mathbf{F}'\|}\langle \mathbf{z}_R|\mathbf{h}_0\rangle\right)^2. \tag{28}$$

In the absence of a signal, each $\langle \mathbf{z}_{L,R}|\mathbf{h}_{0,\pi}\rangle$ follows an independent Gaussian distribution with zero mean and unit variance. This ensures that the terms inside the two brackets in Eq. (28) follow a Gaussian distribution with zero mean and unit variance. This implies that

$$\mathcal{L}^0 \equiv n_1^2 + n_2^2, \qquad \mathcal{L}^\pi \equiv n_3^3 + n_4^2, \tag{29}$$

with $n_{1,2,3,4}$ as standard normal variates,

$$\mathrm{Cov}(n_1, n_3) = \mathrm{Cov}(n_2, n_4) = \frac{\|\mathbf{F}'_+\|^2 - \|\mathbf{F}'_\times\|^2}{\|\mathbf{F}'\|^2} \equiv c,$$
$$\mathrm{Cov}(n_1, n_2) = \mathrm{Cov}(n_3, n_4) = 0. \tag{30}$$

Then the joint distribution of $\sqrt{\mathcal{L}^0}$ and $\sqrt{\mathcal{L}^\pi}$ is a two-dimensional generalized Rayleigh distribution and is given by Eq. (2.1) of [21] as

$$\mathbf{P}(\sqrt{\mathcal{L}^0}, \sqrt{\mathcal{L}^\pi}) = \frac{\sqrt{\mathcal{L}^0\mathcal{L}^\pi}}{c} e^{-\frac{\mathcal{L}^0+\mathcal{L}^\pi}{2(1-c^2)}} I_0\left(\frac{c}{1-c^2}\sqrt{\mathcal{L}^0\mathcal{L}^\pi}\right). \tag{31}$$

This implies that

$$\mathbf{P}(\mathcal{L}^0, \mathcal{L}^\pi) = \frac{1}{4\sqrt{\mathcal{L}^0\mathcal{L}^\pi}} \mathbf{P}(\sqrt{\mathcal{L}^0}, \sqrt{Lc^\pi}) = \frac{1}{4c} e^{-\frac{\mathcal{L}^0+\mathcal{L}^\pi}{2(1-c^2)}} I_0\left(\frac{c}{1-c^2}\sqrt{\mathcal{L}^0\mathcal{L}^\pi}\right). \tag{32}$$

The substitution of Eq. (32) into Eq. (27) gives the distribution of $\mathcal{L}^{mx}$ in the absence of a signal as

$$p_0(\mathcal{L}^{mx}) = \frac{1}{2c} e^{-\frac{\mathcal{L}^{mx}}{2(1-c^2)}} \times \int_0^{\mathcal{L}^{mx}} e^{-\frac{\mathcal{L}^\pi}{2(1-c^2)}} I_0\left(\frac{c}{1-c^2}\sqrt{\mathcal{L}^{mx}\mathcal{L}^\pi}\right) d\mathcal{L}^\pi. \tag{33}$$

In the presence of a signal, for a high multidetector matched filter SNR $\boldsymbol{\rho}_s$, as discussed in Sec. III B, the distribution of $\sqrt{\mathcal{L}^{0,\pi}}$ can be approximated by a Gaussian distribution with a mean $\omega^{0,\pi}\boldsymbol{\rho}_s$ and unit variance. However, for a high $\boldsymbol{\rho}_s$, $\mathcal{L}^{mx} = \mathcal{L}^0$ in the region $0° \le \epsilon \le 70°$, and $\mathcal{L}^{mx} = \mathcal{L}^\pi$ in the region $110° \le \epsilon \le 180°$. Thus, the distribution of $\mathcal{L}^{mx}$ in the presence of a signal can be approximated as

$$p_1(\mathcal{L}^{mx}) \approx \begin{cases} p_1(\mathcal{L}^0), & 0 \le \epsilon < 70°, \\ p_1(\mathcal{L}^\pi), & 110° < \epsilon \le 180°. \end{cases}$$

The FAP and the DP of $\mathcal{L}^{mx}$ can be obtained by numerically integrating $p_0(\mathcal{L}^{mx})$ and $p_1(\mathcal{L}^{mx})$.

In the next section, we carry out numerical simulations to study the statistical properties of $\mathcal{L}$, $\mathcal{L}^{0,\pi}$ and the hybrid statistic $\mathcal{L}^{mx}$. Furthermore, we study the performance of all four statistics in terms of the receiver operator characteristic (ROC) curve for various signal configurations.

V. SIMULATIONS AND DISCUSSION

In this section, we carry out numerical simulations for a three detector network LHV. All of the detectors are assumed to have Gaussian, random noise, with the noise PSDs following a zero-detuning, high power Advanced LIGO noise curve [20]. The GW signal from a nonspinning NS-BH $(2 - 10M_\odot)$ binary system is injected with the SNR $\boldsymbol{\rho}_s = 6$. We assume that the masses are fixed and known for this comparison study. Of course, in a real situation, the masses are unknown and then one needs to place templates in mass space and perform the search. We know that a template based search increases the false alarms. However, this applies to the search based on both the hybrid statistic $\mathcal{L}^{mx}$ and the MLR statistic $\mathcal{L}$, and, further owing to a single stream, we expect to get fewer false alarms for the hybrid statistic compared to the MLR statistic. As mentioned in Sec. I, based on simple arguments on a gravitational wave follow-up of short gamma ray bursts of IPN triggers, in [14] authors used a face-on/face-off tuned MLR statistic (single stream) for nearly on-axis GRBs. This was a targeted search with templates in mass parameter space in LIGO-Virgo data. They did show a similar improvement in the false alarm rates compared to the generic MLR statistic that we got in the fixed mass simulations of the hybrid described below.

The simulation results are as follows. First, we compare the theoretical and numerically evaluated FAPs and DPs for all four statistics, $\mathcal{L}$, $\mathcal{L}^{mx}$, $\mathcal{L}^0$, and $\mathcal{L}^\pi$, and then the performance of the hybrid statistic is compared to the generic MLR statistic, $\mathcal{L}$. This performance is quantified by drawing the ROC plots, i.e, the plot between the FAP and the DP. In each of the plots, the $\mathcal{L}$ statistic is represented by a cyan (solid) line, $\mathcal{L}^{mx}$ by a black (solid) line, $\mathcal{L}^0$ by a red (dashed) line, and $\mathcal{L}^\pi$ by a blue (dash-dotted) line.

A. Comparison of analytical and numerical FAPs and DPs

In Sec. IV, we obtain the analytical expression for distributions of $\mathcal{L}^{mx}$ in the presence and the absence of a signal, i.e., $p_0(\mathcal{L}^{mx})$ and $p_1(\mathcal{L}^{mx})$. Theoretical FAPs and DPs for different thresholds are computed by integrating $p_{0,1}(\mathcal{L}^{mx})$. Here, we compare the theoretical FAPs and DPs with those obtained by numerical simulations.

We generate the network data with 2×10^6 noise realizations with a fixed signal from the NS-BH system located at $(\theta = 140°, \phi = 100°)$ (one of the best locations for a LHV network based on the joint antenna power response), with $\epsilon = \psi = 45°$. For each noise realization, all four $\mathcal{L}$, $\mathcal{L}^{mx}$, $\mathcal{L}^0$, and $\mathcal{L}^\pi$ statistics are computed. For a given threshold £, we count the number of times each of the statistics crosses the threshold value when the data contains only the noise (gives FAP) as well as when the data contains a signal plus noise (gives DP).

Figure 4(a) represents the FAP vs £ for all four statistics. The open circles denote FAPs computed through

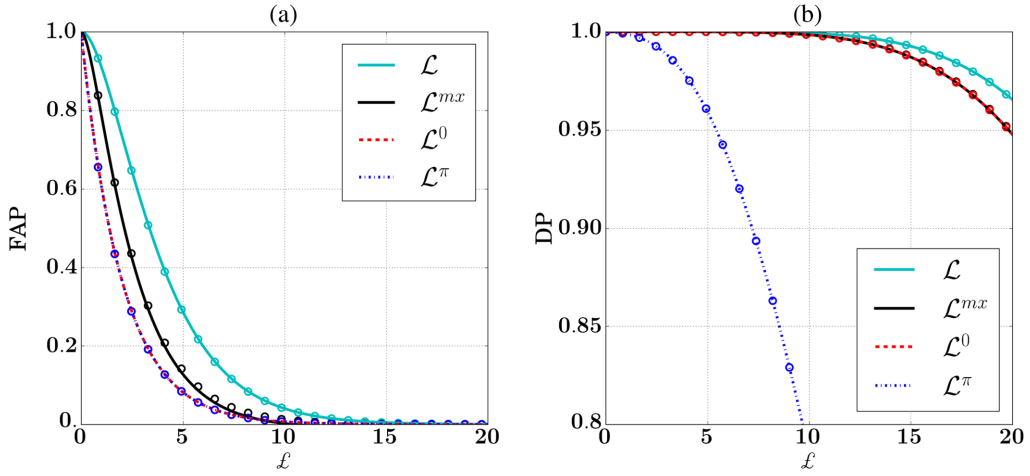

FIG. 4. (a) Variation in FAP of different statistics with respect to the threshold £. (b) Variation in DP of different statistics with respect to the threshold £ for a signal from a $(2-10M_{\odot})$ nonspinning NS-BH binary system with $\boldsymbol{\rho}_s = 6$ optimally located at ($\theta = 140°$, $\phi = 100°$), with an arbitrary $\epsilon = 45°$ and $\Psi = 45°$. The curves are generated from the theory and circles are from simulations. We assume zero-detuning, high power Advanced LIGO PSDs [20] for all detectors.

simulations, as detailed above, whereas the continuous lines denote the theoretically obtained FAPs. We observe a remarkable agreement of the analytical result with the numerical simulation. The main result derived and understood from Fig. 4(a) is the difference in the FAP values corresponding to a given threshold for various statistics. Owing to two data streams, $\mathcal{L}$ gives the maximum FAP amongst all four. Since $\mathcal{L}^{0,\pi}$ are constructed out of a single synthetic stream, the FAPs of both are identical and are the least amongst the four. Since the hybrid statistic is constructed as $\mathcal{L}^{0,\pi}$, its FAP is slightly higher than that of $\mathcal{L}^{0,\pi}$.

Figure 4(b) represents the DP vs £ for all four statistics. The open circles denote the DPs from simulations, whereas the continuous lines denote the theoretical DPs. Since the DPs for all four statistics depend on the fractional optimal SNRs captured by the individual statistic, the DP of $\mathcal{L}$ is maximum as it captures $\boldsymbol{\rho}_s$ in the no noise case. For the signal with $\epsilon = 45°$, $\mathcal{L}^{mx}$ is $\mathcal{L}^{0}$ most of the time; thus, the DPs of $\mathcal{L}^{mx}$ and $\mathcal{L}^{0}$ overlap. The statistic $\mathcal{L}^{\pi}$ captures a small fraction of the $\boldsymbol{\rho}_s$ (see Fig. 3) and hence shows the least DP. Once again, we see remarkable agreement between the numerically computed DPs and the analytically integrated DPs for all of the statistics.

B. Performance of hybrid statistic for a single injection

In this subsection, we study the performance of $\mathcal{L}^{mx}$ against the rest of the statistics—most importantly, the generic multidetector MLR statistic $\mathcal{L}$.

We generate the network data with 2×10^6 noise realizations and a fixed signal from a NS-BH system optimally located at ($\theta = 140°$, $\phi = 100°$), with an arbitrary $\psi = 45°$ but varying binary inclination. We select six binary inclination angles—namely, $\epsilon = 0°, 45°, 70°, 90°$, 135°, and 180°—and obtain the ROC curves numerically, as shown in Figs. 5(a)–5(e), and 5(f), respectively. We summarize the results below.

For the $\epsilon = 0$ or π case, $\mathcal{L}^{mx}$ (being optimized for the face-on/face-off case) is expected to perform better than the generic MLR statistic. Figures 5(a) and 5(e) show the same. As discussed earlier, this improvement is primarily due to the reduction in the FAP of $\mathcal{L}^{mx}$. For a fixed FAP of 10^{-5}, the subsequent improvement in the DP is 6%, which translates to an increase in the detection rate of 6%.

For the $\epsilon = 45°$ or 135° case (symmetrically located from the 0 and π cases, respectively), as seen in Figs. 5(b) and 5(e), the improvement in the ROC of $\mathcal{L}^{mx}$ compared to that of $\mathcal{L}$ is similar. This improvement is due to the drop in the FAP of $\mathcal{L}^{mx}$. As shown in Appendix B, at $\epsilon = 45°$, the $\mathcal{L}^{mx}$ captures the entire optimum SNR. Thus, the improvement in the DP remains close to 6%, similar to the face-on/face-off case.

Following the above argument, as ϵ approaches the edge-on case, the fractional SNR captured in $\mathcal{L}^{mx}$ reduces. Thus, the ROC of $\mathcal{L}^{mx}$ starts approaching the ROC of $\mathcal{L}$, as seen in Fig. 5(c). Here, the improvement of $\mathcal{L}^{mx}$ is 2% over the $\mathcal{L}$.

For the $\epsilon = 90°$ case, the fractional optimal SNR captured by $\mathcal{L}^{mx}$ is very small as $\mathcal{L}^{mx}$ is optimized for the face-on/face-off case. Thus, the MLR statistic performs better than the $\mathcal{L}^{mx}$ at the edge-on case, as shown in Fig. 3(d)

C. Performance of the hybrid statistic for injections sampled from a distribution

In this simulation, we generate the network data with 2×10^6 noise realizations and signals from a NS-BH system with masses $(2-10M_{\odot})$ and multidetector SNR $\rho_s = 6$. We randomly draw the binary inclination angle ϵ,

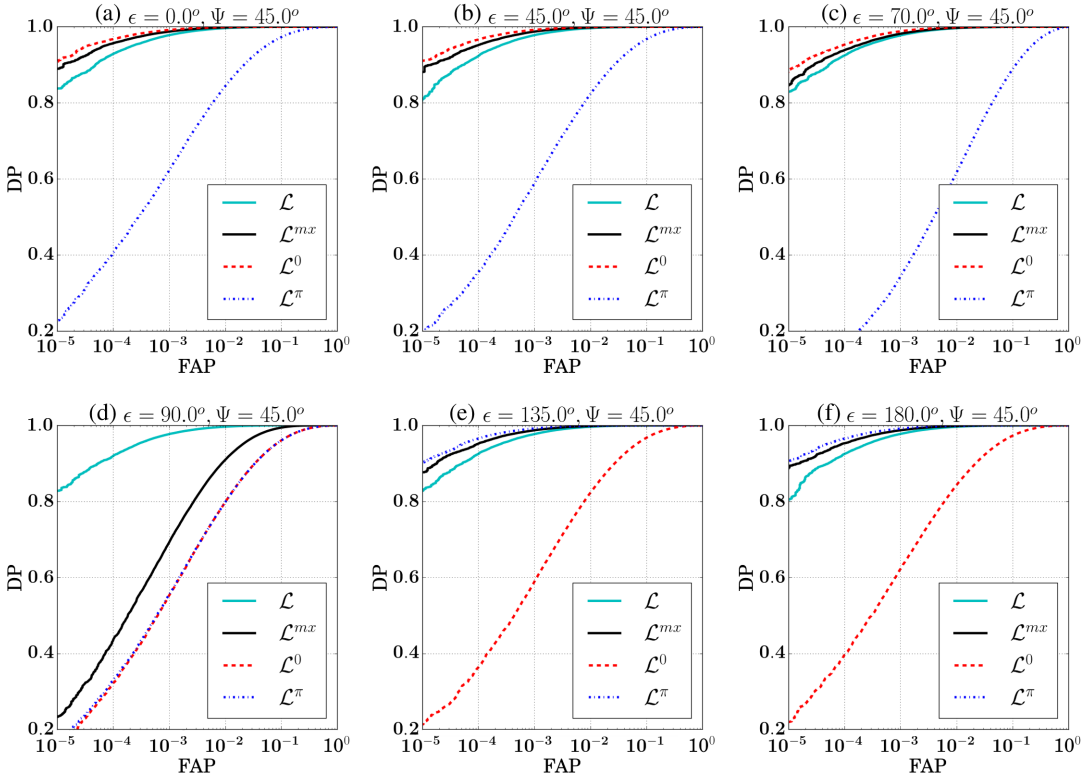

FIG. 5. ROC plots of the four statistics corresponding to a network LHV for fixed injections with different values of ε; (a) $\varepsilon = 0°$, (b) $\varepsilon = 45°$, (c) $\varepsilon = 70°$, (d) $\varepsilon = 90°$, (e) $\varepsilon = 135°$, and (f) $\varepsilon = 180°$. The signal with the SNR $\boldsymbol{\rho}_s = 6$ is from the $(2 - 10M_\odot)$ NS-BH system optimally located at ($\theta = 140°$, $\phi = 100°$), with an arbitrary polarization angle $\psi = 45°$. We assume zero-detuning, high power Advanced LIGO PSDs [20] for all detectors.

polarization angle Ψ, and source location (θ, ϕ) from a given distribution. We perform this exercise for two distinct distributions, Dist. 1 and Dist. 2 of inclination angle ϵ. In both cases, $\cos\theta$, ϕ, and Ψ are sampled uniformly from the intervals $[-1, 1]$, [0°, 360°], and [0°, 90°], respectively.

Dist. 1 draws $\cos(\epsilon)$ uniformly from $[-1, 1]$ and is denoted by a green (solid) line in Fig. 6(a). As seen in the figure, the population of random samples drawn from this distribution contains more edge-on sources than face-on ones.

In Dist. 2, the ϵ follows the distribution proposed in Eq. (28) of [22] [see the green (dashed) line in Fig. 6(a)],

$$\mathbf{P}(\epsilon) = 0.076076(1 + 6\cos^2\epsilon + \cos^4\epsilon)^{3/2}\sin\epsilon. \quad (34)$$

Dist. 2 is a realistic distribution of ϵ, where the SNR information is folded into the distribution, along with the geometric prior. Since we know that the edge-on sources have a lower SNR than face-on sources, we expect to see a lesser number of edge-on systems than face-on ones. As a

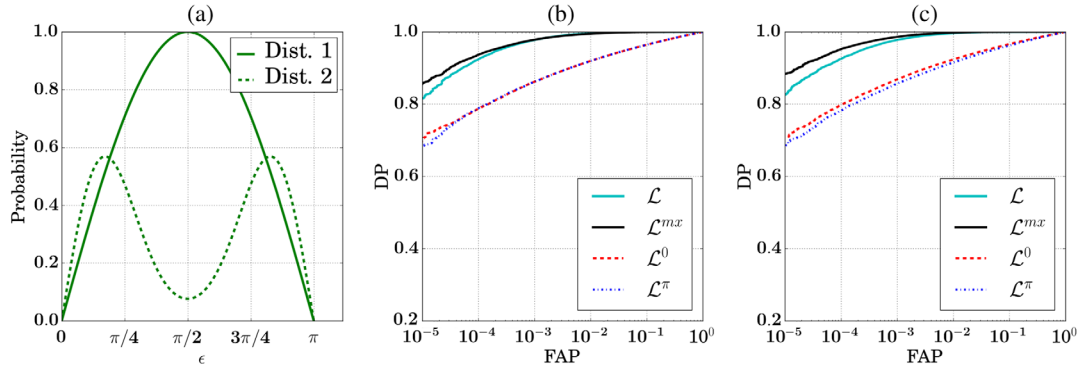

FIG. 6. (a) Plot of two sampling distributions of ϵ. (b) ROC plots for four different statistics corresponding to a network LHV when the injected signal's inclination angle, ϵ drawn from Dist. 1. (c) ROC plots for injections with ε drawn from Dist. 2. In both cases, sky location and polarization angle are sampled uniformly. The injections are with the SNR $\boldsymbol{\rho}_s = 6$ and are from the $(2 - 10M_\odot)$ NS-BH system. We assume zero-detuning, high power Advanced LIGO PSDs [20] for all detectors.

result, there would be a dip in the curve (the dashed line) with respect to the Dist. 1 (the solid line).

Figures 6(b) and 6(c) summarize the results in terms of the ROC curves using Dist. 1 and Dist. 2, respectively. The ROC curve summarizes the performance of the MLR statistic compared to the hybrid statistic averaged over all of the source locations and the polarizations.

Figure 6(b) shows that, for Dist. 1, the average performance of $\mathcal{L}^{mx}$ is better than that of $\mathcal{L}$ in spite of a greater number of sources located around the edge-on source. Quantitatively, DP improves by ∼5% for the FAP 10^{-5}.

However, Fig. 6(c) shows a more realistic performance, as we expect the inclination angle distribution to be more realistic in this case. We note that, for Dist. 2, the hybrid statistic performs much better than the MLR statistic $\mathcal{L}$. Quantitatively, for a FAP of 10^{-5}, $\mathcal{L}^{mx}$ improves the DP by 7% over $\mathcal{L}$.

D. Conclusion and future directions

In this article, we revisit the CBC GW search problem with a multidetector network consisting of advanced interferometers like LIGO-Virgo in a coherent approach. We show that the hybrid statistic constructed from two statistics; namely, coherent MLR statistics tuned for face-on and face-off binaries captures most of the multidetector optimum SNR for a large fraction of the binary inclination angles, except for a small window centered around the edge-on case. The statistical properties of this hybrid statistic are studied in detail. The performance of this hybrid statistic is compared with that of the coherent MLR statistic for generic inclination angles. Being constructed from the single synthetic data stream, the hybrid statistic gives fewer false alarms compared to the two stream generic multidetector MLR statistic and a very small fractional loss in the optimum SNR for a large range of binary inclinations.

We have demonstrated the performance by using the noise model as Gaussian with zero-detuning, high power Advanced LIGO PSDs [20] in a LHV network for the NS-BH system of masses $(2-10M_{\odot})$ for a fixed SNR of 6. The ROC curves are used as a tool for this demonstration. The simulations are performed for two cases.

Case 1.—The source is optimally located in the LHV network and is oriented with various binary inclination angles. The ROC curves show that the hybrid statistic performs better than the generic MLR statistic for all inclination angles less then 70° and greater than 110°. The improvement in each of them corresponds to two factors. First, the hybrid statistic captures most of the optimum SNR for a large region of inclination and polarization parameter space. Thus, we do not lose much in the DP for a given multidetector matched filter SNR ρ_s. Furthermore, by construction, the hybrid statistic is out of a single stream. Thus, the FAP of the hybrid statistic is better than that of the two stream generic MLR statistic (of course, it is slightly worse than the pure single streams $\mathcal{L}^0$ and $\mathcal{L}^{\pi}$).

Case 2.—The source location as well as the orientation and the polarization are sampled from a distribution. The source location is sampled uniformly from the sky sphere. The polarization angle follows a uniform distribution. The inclination angles are drawn from two distributions, namely, $U[\cos(\epsilon)]$ and a more realistic distribution proposed in [22]. The ROC curve shows that the performance of the hybrid statistic gives an improvement of ∼5% and ∼7%, respectively, in DP compared to the generic multidetector MLR statistic for a fixed FAP of 10^{-5}.

In [14], the authors applied a similar statistic for the SGRB follow-up search for very small inclination angles. However, this study and its performance in Gaussian noise clearly shows that the hybrid statistic would give a better performance for a wide range of inclination angles, barring a small window around the edge-on case. Since we expect that the source population would have a bias towards the face-on/face-off cases due to the relative difference in the SNRs, this statistic would play a crucial role in the multidetector CBC search in the advanced era.

We plan to apply this to the S6 noise of the science run of LIGO detectors and to test the performance of the statistic for generic inclination angles. We also plan to extend the study to a larger network, which includes LIGO-India and KAGRA.

ACKNOWLEDGMENTS

The authors availed themselves of the 128 core computing facility established by the MPG-DST Max Planck Partner Group at IISER TVM. The authors would like to thank S. Fairhurst for reviewing the draft and for the useful comments.

APPENDIX A: RELATION BETWEEN $\{A,\phi_a,\epsilon,\Psi\}$ AND $\{\rho_L,\rho_R,\Phi_L,\Phi_R\}$

The new parameters $\{\rho_L,\rho_R,\Phi_L,\Phi_R\}$ are related to the physical parameters $\{A,\phi_a,\epsilon,\Psi\}$ as

$$\rho_L e^{i\Phi_L} = A\|\mathbf{F}'_+\|e^{i\phi_a}\left[\frac{1+\cos^2\epsilon}{2}\cos 2\chi + i\cos\epsilon\sin 2\chi\right],$$
$$\rho_R e^{i\Phi_R} = A\|\mathbf{F}'_\times\|e^{i\phi_a}\left[\frac{1+\cos^2\epsilon}{2}\sin 2\chi - i\cos\epsilon\cos 2\chi\right]. \tag{A1}$$

The absolute values and the phases of the above equations are $\{\rho_L,\rho_R,\Phi_L,\Phi_R\}$ and are explicitly given in Eq. (B1) of [13].

APPENDIX B: $\mathcal{L}^{0,\pi}$ IN THE ABSENCE OF NOISE

In this section we derive the expression for the fraction of the multidetector matched filter SNR captured by the statistics $\mathcal{L}^0$ and $\mathcal{L}^{\pi}$.

From Eqs. (5) and (18), $\mathbf{z}^{0,\pi}$ can be reexpressed in terms of $\mathbf{z}_{L,R}$ as

$$\tilde{\tilde{z}}^{0,\pi}(f) = \frac{\|\mathbf{F}'_+\|}{\|\mathbf{F}'\|}\tilde{\tilde{z}}_L(f) \pm i\frac{\|\mathbf{F}'_\times\|}{\|\mathbf{F}'\|}\tilde{\tilde{z}}_R(f), \tag{B1}$$

where $+$ corresponds to $\mathbf{z}^0$ and $-$ corresponds to $\mathbf{z}^\pi$. By substituting back into Eq. (19), $\mathcal{L}^{0,\pi}$ can be expanded in terms of the four terms $\langle \mathbf{z}_{L,R}|\mathbf{h}_{0,\pi}\rangle$:

$$\mathcal{L}^{0,\pi} = \left(\frac{\|\mathbf{F}'_+\|}{\|\mathbf{F}'\|}\langle \mathbf{z}_L|\mathbf{h}_0\rangle \pm \frac{\|\mathbf{F}'_\times\|}{\|\mathbf{F}'\|}\langle \mathbf{z}_R|\mathbf{h}_{\pi/2}\rangle\right)^2 + \left(\frac{\|\mathbf{F}'_+\|}{\|\mathbf{F}'\|}\langle \mathbf{z}_L|\mathbf{h}_{\pi/2}\rangle \mp \frac{\|\mathbf{F}'_\times\|}{\|\mathbf{F}'\|}\langle \mathbf{z}_R|\mathbf{h}_0\rangle\right)^2. \tag{B2}$$

Using Eqs. (1) and (A1), the scalar products in the above equation in the absence of noise can be written

$$\begin{aligned}
&\langle \mathbf{z}_L|\mathbf{h}_0\rangle|_{\mathbf{n}=0} = \Re[\boldsymbol{\rho}_L e^{i\Phi_L}], \quad \langle \mathbf{z}_L|\mathbf{h}_{\pi/2}\rangle|_{\mathbf{n}=0} = -\Im[\boldsymbol{\rho}_L e^{i\Phi_L}],\\
&\langle \mathbf{z}_R|\mathbf{h}_0\rangle|_{\mathbf{n}=0} = \Re[\boldsymbol{\rho}_R e^{i\Phi_R}], \quad \langle \mathbf{z}_R|\mathbf{h}_{\pi/2}\rangle|_{\mathbf{n}=0} = -\Im[\boldsymbol{\rho}_R e^{i\Phi_R}].
\end{aligned} \tag{B3}$$

Substituting in Eq. (B2) gives

$$\mathcal{L}^{0,\pi}|_{\mathbf{n}=0} = \left|\frac{\|\mathbf{F}'_+\|}{\|\mathbf{F}'\|}\boldsymbol{\rho}_{Ls}e^{i\Phi_{Ls}} \pm i\frac{\|\mathbf{F}'_\times\|}{\|\mathbf{F}'\|}\boldsymbol{\rho}_{Rs}e^{i\Phi_{Rs}}\right|^2. \tag{B4}$$

We further expand Eq. (B4) in terms of the physical parameters to obtain the explicit dependence on ϵ for a fixed SNR case:

$$\begin{aligned}
\mathcal{L}^{0,\pi}|_{\mathbf{n}=0} &= \frac{\mathrm{A}^2}{\|\mathbf{F}'\|^2}\left|\|\mathbf{F}'_+\|^2\left(\frac{1+\cos^2\epsilon}{2}\cos 2\chi + i\cos\epsilon\sin 2\chi\right)\right.\\
&\quad \left. \pm i\|\mathbf{F}'_\times\|^2\left(\frac{1+\cos^2\epsilon}{2}\sin 2\chi - i\cos\epsilon\cos 2\chi\right)\right|^2\\
&= \frac{\mathrm{A}^2}{\|\mathbf{F}'\|^2}\left[\mathrm{T}_1\left(\frac{1+\cos^2\epsilon}{2}\right)^2 + \mathrm{T}_2\cos^2\epsilon \right.\\
&\quad \left. \pm \mathrm{T}_3\frac{1+\cos^2\epsilon}{2}\cos\epsilon\right],
\end{aligned} \tag{B5}$$

where the three terms T_1, T_2, and T_3 are defined as

$$\begin{aligned}
\mathrm{T}_1 &\equiv \|\mathbf{F}'_+\|^4\cos^2 2\chi + \|\mathbf{F}'_\times\|^4\sin^2 2\chi,\\
\mathrm{T}_2 &\equiv \|\mathbf{F}'_+\|^4\sin^2 2\chi + \|\mathbf{F}'_\times\|^4\cos^2 2\chi,\\
\mathrm{T}_3 &\equiv 2\|\mathbf{F}'_+\|^2\|\mathbf{F}'_\times\|^2.
\end{aligned} \tag{B6}$$

To obtain a fixed multidetector matched filter SNR $\boldsymbol{\rho}_s$, face-on binaries should be kept at a larger distance than the edge-on binaries. This is because the face-on binaries carry more polarization power than the edge-on ones. This is reflected in the derived amplitude, A, in Eq. (B5) as

$$\mathrm{A}^2 = \frac{\boldsymbol{\rho}_s^2}{\mathrm{R}_1\left(\frac{1+\cos^2\epsilon}{2}\right)^2 + \mathrm{R}_2\cos^2\epsilon}, \tag{B7}$$

with

$$\begin{aligned}
\mathrm{R}_1 &= \|\mathbf{F}'_+\|^2\cos^2 2\chi + \|\mathbf{F}'_\times\|^2\sin^2 2\chi,\\
\mathrm{R}_2 &= \|\mathbf{F}'_+\|^2\sin^2 2\chi + \|\mathbf{F}'_\times\|^2\cos^2 2\chi.
\end{aligned} \tag{B8}$$

A substitution of Eq. (B7) into Eq. (B5) gives the fraction $\omega^{0,\pi}$ of $\boldsymbol{\rho}_s$, captured by the $\mathcal{L}^{0,\pi}$ statistic in the absence of noise:

$$\begin{aligned}
(\omega^{0,\pi})^2 &\equiv \frac{\mathcal{L}^{0,\pi}|_{\mathbf{n}=0}}{\boldsymbol{\rho}_s^2}\\
&= \frac{\mathrm{T}_1\left(\frac{1+\cos^2\epsilon}{2}\right)^2 + \mathrm{T}_2\cos^2\epsilon \pm \mathrm{T}_3\frac{1+\cos^2\epsilon}{2}\cos\epsilon}{\|\mathbf{F}'\|^2[\mathrm{R}_1\left(\frac{1+\cos^2\epsilon}{2}\right)^2 + \mathrm{R}_2\cos^2\epsilon]}.
\end{aligned} \tag{B9}$$

Please note that, for the face-on/face-off case, $\omega^{0,\pi} = 1$. However, as we see in Fig. 3, we expect the ω^0 to drop as the signal ϵ increases from 0 and, similarly, we expect ω^π to drop as the signal ϵ drops from π.

In Eq. (B9), the inclination angle ϵ appears in terms of $\cos\epsilon$ and $\frac{1+\cos^2\epsilon}{2}$. If we expand $\cos\epsilon$ about $\epsilon = 0$ up to fourth order, then

$$\begin{aligned}
\cos\epsilon &\approx 1 - \frac{\epsilon^2}{2} + \frac{\epsilon^4}{24} \equiv \mathrm{Ce},\\
\frac{1+\cos^2\epsilon}{2} &\approx 1 - \frac{\epsilon^2}{2} + \frac{4\epsilon^4}{24}.
\end{aligned} \tag{B10}$$

A substitution of Eq. (B10) into the expression for ω^0 gives

$$\begin{aligned}
(\omega^0)^2 &= \left(1 + \frac{\mathrm{T}_1 + \mathrm{T}_3/2}{4\|\mathbf{F}'\|^4\mathrm{Ce}}\epsilon^4\right)\Big/\left(1 + \frac{\mathrm{R}_1}{4\|\mathbf{F}'\|^2\mathrm{Ce}}\epsilon^4\right)\\
&\approx \left(1 + \frac{\mathrm{T}_1 + \mathrm{T}_3/2}{4\|\mathbf{F}'\|^4\mathrm{Ce}}\epsilon^4\right)\left(1 - \frac{\mathrm{R}_1}{4\|\mathbf{F}'\|^2\mathrm{Ce}}\epsilon^4\right)\\
&\approx 1 + \frac{\epsilon^4}{\mathrm{Ce}\|\mathbf{F}'\|^4}(\mathrm{T}_1 + \mathrm{T}_3/2 - \|\mathbf{F}'\|^2\mathrm{R}_1),
\end{aligned} \tag{B11}$$

Here, we make use of the identities $\mathrm{T}_1 + \mathrm{T}_2 + \mathrm{T}_3 = \|\mathbf{F}'\|^4$ and $\mathrm{R}_1 + \mathrm{R}_2 = \|\mathbf{F}'\|^2$ from Eqs. (B6) and (B8). Again, from Eqs. (B6) and (B8),

$$\mathrm{T}_1 + \mathrm{T}_3/2 - \|\mathbf{F}'\|^2\mathrm{R}_1 = 0. \tag{B12}$$

This implies that

$$\omega^0 = 1. \tag{B13}$$

The fourth order approximation of the $\cos\epsilon$ given in Eq. (B10) is valid for a wide range of ϵ's. For $\epsilon \leq 70°$, the error in this approximation is less than 1.5%. Thus, we can safely assume that $\omega^0 \approx 1$ for $0° \leq \epsilon \leq 70°$. For example, Table I gives the minimum values of ω^o over Ψ for various

TABLE I. Minimum value of ω^o over Ψ for various ϵ's in a network LHV. The signal is from the $(2-10M_\odot)$ NS-BH system located at $(\theta = 140°, \phi = 100°)$. We assume zero-detuning, high power Advanced LIGO PSDs [20] for all detectors.

Binary inclination, ϵ	50°	60°	70°	80°
Minimum value of ω^0	0.999	0.995	0.98	0.87

ϵ's in a network LHV for a signal from the $(2-10M_\odot)$ NS-BH system located at $(\theta = 140°, \phi = 100°)$.

Similarly, by expanding $\cos\epsilon$ about π, it can be easily shown that for $110° \leq \epsilon \leq 180°$, $\omega^\pi \approx 1$. Figures 2 and 3 justify the above claim.

For edge-on binaries at $\chi = 45°$ (please note that $\chi = \Psi - \delta/4$, as defined in Sec. II), from Eq. (B9) the SNR fraction captured by $\mathcal{L}^{0,\pi}$ becomes

$$\omega^{0,\pi} = \frac{\|\mathbf{F}'_\times\|}{\|\mathbf{F}'\|}. \tag{B14}$$

In other words, at this point $\boldsymbol{\rho}_L$ vanishes and the entire network SNR is accumulated in the SNR, $\boldsymbol{\rho}_R$ of the subdominant stream $\mathbf{z}_R$. Since, by construction of the dominant polarization frame, $\|\mathbf{F}'_\times\|$ is less than $\|\mathbf{F}_+{}'\|$, this results in a minimum $\omega^{0,\pi}$.

[1] J. Aasi, B. P. Abbott, R. Abbott, T. Abbott, M. R. Abernathy, K. Ackley, C. Adams, T. Adams, P. Addesso *et al.* (LIGO Scientific Collaboration), Advanced LIGO, Classical Quantum Gravity **32**, 074001 (2015).

[2] G. M. Harry (LIGO Scientific Collaboration), Advanced LIGO: The next generation of gravitational wave detectors, Classical Quantum Gravity **27**, 084006 (2010).

[3] B. P. Abbott, R. Abbott, T. D. Abbott, M. R. Abernathy, F. Acernese, K. Ackley, C. Adams, T. Adams, P. Addesso, R. X. Adhikari *et al.* (LIGO Scientific and Virgo Collaborations), Observation of Gravitational Waves from a Binary Black Hole Merger, Phys. Rev. Lett. **116**, 061102 (2016).

[4] F. Acernese *et al.* (Virgo Collaboration), Advanced Virgo: A second-generation interferometric gravitational wave detector, Classical Quantum Gravity **32**, 024001 (2015).

[5] T. Accadia *et al.* (Virgo Collaboration), Report No. VIR-0128A-12, 2012.

[6] Y. Aso, Y. Michimura, K. Somiya, M. Ando, O. Miyakawa, T. Sekiguchi, D. Tatsumi, and H. Yamamoto (KAGRA Collaboration), Interferometer design of the KAGRA gravitational wave detector, Phys. Rev. D **88**, 043007 (2013).

[7] K. Somiya, Detector configuration of KAGRA–the Japanese cryogenic gravitational-wave detector, Classical Quantum Gravity **29**, 124007 (2012).

[8] B. Iyer *et al.* (LIGO Collaboration), Report No. LIGO-M1100296-v2, 2011.

[9] J. Abadie, B. P. Abbott, R. Abbott, M. Abernathy, T. Accadia, F. Acernese, C. Adams, R. Adhikari, P. Ajith, B. Allen *et al.*, Predictions for the rates of compact binary coalescences observable by ground-based gravitational-wave detectors, Classical Quantum Gravity **27**, 173001 (2010).

[10] C. W. Helstrom, *Statistical Theory of Signal Detection* (Pergamon Press, New York, 1960).

[11] A. Pai, S. Dhurandhar, and S. Bose, Data-analysis strategy for detecting gravitational-wave signals from inspiraling compact binaries with a network of laser-interferometric detectors, Phys. Rev. D **64**, 042004 (2001).

[12] I. W. Harry and S. Fairhurst, Targeted coherent search for gravitational waves from compact binary coalescences, Phys. Rev. D **83**, 084002 (2011).

[13] K. Haris and A. Pai, Synthetic streams in a gravitational wave inspiral search with a multidetector network, Phys. Rev. D **90**, 022003 (2014).

[14] A. Williamson, C. Biwer, S. Fairhurst, I. Harry, E. Macdonald, D. Macleod, and V. Predoi, Improved methods for detecting gravitational waves associated with short gamma-ray bursts, Phys. Rev. D **90**, 122004 (2014).

[15] T. B. Littenberg and N. J. Cornish, Bayesian approach to the detection problem in gravitational wave astronomy, Phys. Rev. D **80**, 063007 (2009).

[16] C. Cutler and B. F. Schutz, Generalized $\mathcal{F}$-statistic: Multiple detectors and multiple gravitational wave pulsars, Phys. Rev. D **72**, 063006 (2005).

[17] R. Prix and B. Krishnan, Targeted search for continuous gravitational waves: Bayesian versus maximum-likelihood statistics, Classical Quantum Gravity **26**, 204013 (2009).

[18] P. Jaranowski, A. Królak, and B. F. Schutz, Data analysis of gravitational-wave signals from spinning neutron stars: The signal and its detection, Phys. Rev. D **58**, 063001 (1998).

[19] S. Klimenko, S. Mohanty, M. Rakhmanov, and G. Mitselmakher, Constraint likelihood analysis for a network of gravitational wave detectors, Phys. Rev. D **72**, 122002 (2005).

[20] D. Shoemaker *et al.* (LIGO Collaboration), Report No. LIGO-T0900288-v3, 2010.

[21] L. E. Blumenson and K. S. Miller, Properties of generalized rayleigh distributions, Ann. Math. Stat. **34**, 903 (1963).

[22] B. F. Schutz, Networks of gravitational wave detectors and three figures of merit, Classical Quantum Gravity **28**, 125023 (2011).